Investigation of Contact Properties and Device Performance for Bifacial Double-Side Textured Silicon Solar Cells With Polysilicon Based Passivating Contacts

Pradeep Padhamnath[1] [ID], John Derek Arcebal [1] [ID], Sagnik Dasgupta[2] [ID], Gabby De Luna[1] [ID], Ajeet Rohatgi[2] [ID], and Armin G. Aberle [1] [ID]

[1]National University of Singapore, Singapore

[2] Georgia Institute of Technology, USA

Abstract. We investigate the impact of the surface morphology on the contact properties of phosphorus doped poly-Si layers. If the poly-Si layer on a textured surface remains intact after high-temperature metallization using a fire-through (FT) silver (Ag) paste, the $J_{0,metal}$ is not expected to increase significantly while the specific contact resistivity can improve with a textured surface. The contact properties of the FT Ag contacts to n^+ poly-Si deposited on both textured and planar surfaces are investigated by measuring and evaluating ρ_c and $J_{0,metal}$. The reasons for differences in contact resistance and recombination are further investigated with SEM imaging. Solar cells with n-type polysilicon based passivating contacts on the rear side are fabricated and characterized. The scientific approach used, and the insights presented in this work, help to understand the mechanisms and behavior of screen-printed and fired-through contacts to polysilicon layers deposited onto textured silicon surfaces.

Keywords: Passivated Contacts, Polysilicon, Metallization

1. Introduction

Phosphorus doped polysilicon (n^+ poly-Si) based passivating contacts of silicon solar cells have been the most widely researched and successfully implemented by both industry and academia [1, 2]. This can be attributed to the better passivation properties observed with n^+ poly-Si as compared to p^+ poly-Si, as recently reported in the literature [3, 4]. Consequently, fire-through (FT) contacts to n^+ poly-Si using Ag paste were the first to be implemented commercially. Parasitic light absorption in the poly-Si layers [5, 6] has limited their application to the rear side of the bifacial solar cells, where texturing of the surface is not mandatory [7, 8]. However, there has been a growing interest in recent years in the application of poly-Si based contacts on both the front and rear side of the solar cells [9-11]. Therefore, analysis of metal contacts with poly-Si is also helpful for solar cells with passivated contacts applied to the front side of the double-side passivated contact solar cells.

Properties of the contacts formed with fire-through pastes with n^+ poly-Si deposited on planar surfaces were studied previously [12-15]. Despite the widespread use of FT Ag pastes for making contacts to n^+ poly-Si, the interactions of the metal paste with the doped poly-Si layer deposited on *textured* surfaces have only recently been investigated. In a recently published work researchers reported a contact resistivity of 2.7 mΩ-cm^2 and a high saturation current of 480 fA/cm^2 for screen-printed Ag contacts to poly-Si deposited on textured surfaces

[16]. Another work investigated the impact of the paste on different surface finishes such as saw damage etched, chemically polished after texturing and textured surfaces, and found that the contact properties on planar surfaces outperform the contact properties on textured surfaces [17]. However, double-side textured solar cells are expected to have improved annual energy yield, especially for bifacial cell architectures. In another recent publication, several rear surface morphologies were investigated for optimum solar cell performance [18].

In this work, we investigate whether a change in the surface morphology can improve the contacting of poly-Si layers. If the poly-Si layer on a textured silicon surface remains intact after the etching by the FT Ag paste, the $J_{0,metal}$ is not expected to increase significantly while the ρ_c could improve with a textured surface. The contact properties of the FT Ag contacts to n^+ poly-Si deposited on both textured and planar surface are investigated by measuring and evaluating ρ_c and $J_{0,metal}$. The reasons for differences in contact resistance and recombination are further investigated with SEM imaging. Solar cells with n-type polysilicon based passivating contacts on the rear side are fabricated and characterized. The scientific approach used, and the insights presented in this work, help to understand the mechanisms and behavior of screen-printed and fired-through contacts to polysilicon layers deposited onto textured silicon surfaces.

2. Experimental Details

Samples and solar cells are fabricated on large-area (1.2 Ω-cm, M2, 15.6x15.6 cm^2) n-type silicon wafers. Some p-type test wafers were also used to prepare the test samples used for measuring sheet resistances (R_{sheet}), the active dopant profile and specific contact resistivity (ρ_c). Test samples are either symmetrically polished in KOH (20%) or symmetrically textured in KOH (2%) solution. The passivated contact was formed by thermally growing the interfacial oxide layer (iO_x) and deposition of 150 nm intrinsic poly-Si in a single process in a horizontal tube low-pressure chemical vapour deposition system (LPCVD) [4]. The poly-Si layer was then doped in a horizontal tube diffusion furnace using $POCl_3$ as the dopant source. After removing the phosphosilicate glass and wet chemical cleaning, 70 nm of hydrogenated silicon nitride (SiN_x) was deposited using inline plasma enhanced chemical vapour deposition (PECVD). The process followed for fabricating single side passivated contact solar cells is explained in detail in our earlier work [14]. All fabricated solar cells have a boron diffused front surface passivated by 10nm aluminum oxide layer (AlO_x) followed by deposition of 50 nm SiN_x as anti-reflection coating (ARC). The doped poly-Si layer on the rear side was covered with a single 70 nm layer of hydrogenated silicon nitride similar to the layer on the test samples. All these layers were deposited using an inline PECVD tool. Contacts to the n^+ poly-Si and p^+ c-Si are formed with commercially available Ag pastes and Ag/Al pastes, respectively, using screen printing and firing at high temperature. The sheet resistance of the doped poly-Si layers was mapped across the whole area using a four-point probe tool. The active dopant concentration was measured using an electrochemical capacitance voltage (ECV) measurement tool. The passivation quality of the doped poly-Si/iO_x passivated contact layer was determined using the quasi-steady-state photoconductance (QSSPC) measurement method. The specific contact resistivity (ρ_c) was measured using the modified transfer length measurement (TLM) method and the saturation current density under the metal contacts ($J_{0,metal}$) was evaluated by finite element modelling (FEM) of photoluminescence (PL) images as explained in a previous work [13]. The FEM on the PL images was implemented with the help of Griddler software. Details regarding the model, nodes and the underlying equations could be found in [13]. To further understand the behaviour of the contact, the metal contacts are etched, and the analysis is done using scanning electron microscopy and image analysis. The contacts were first etched in nitric acid to remove the bulk metal, after which the glass interlayer was visible. Some samples were removed at this point for observation. Other samples were treated with hydrofluoric acid to remove the glass interlayer to observe the metal crystallites embedded in the poly-Si layer. Finally, the samples were treated again with nitric acid to remove the metal crystallites embedded in poly-Si layer to observe the etch pits made by the high temperature fire-through contacts. Finally, solar cells are fabricated and characterized.

3. Experimental results and Discussion

3.1 Electrical properties of the *n$^+$* poly-Si layers

Figures 1 and 2 show the active dopant profiles and the R_{sheet}, respectively, of 150-nm *n$^+$* poly-Si layers deposited on planar and textured samples. From the ECV measurements of both planar and textured samples, the apparent thickness of the poly-Si layer – which is the depth beyond which the dopant concentration falls at a much faster rate than the 'flat-band' region near the surface – is similar for both planar and textured surfaces. The area factor used in ECV measurements was the same as that used for the LPCVD deposition (1.4). Hence, the thickness of poly-Si was similar for both planar and textured surfaces. Figure 2 shows the R_{sheet} measured on both planar and textured samples. S1 and S2 denote to the samples placed at the beginning and the end of the samples processed together in the LPCVD and diffusion furnaces. R_{sheet} is similar for both textured and planar samples, which again indicates that the thicknesses of the poly-Si layers on both planar and textured samples are similar.
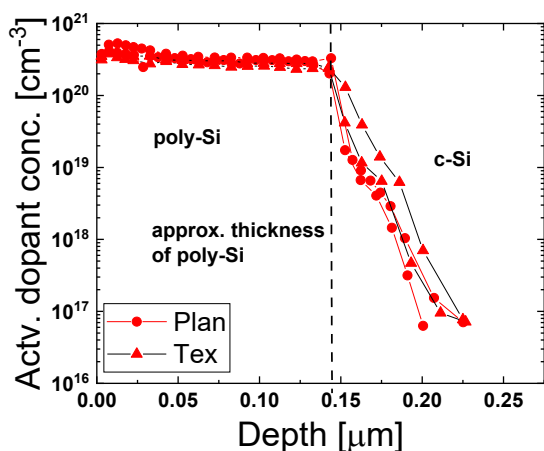

***Figure 1**: ECV profiles for 150 nm thick n$^+$ poly-Si deposited on planar and textured samples.*
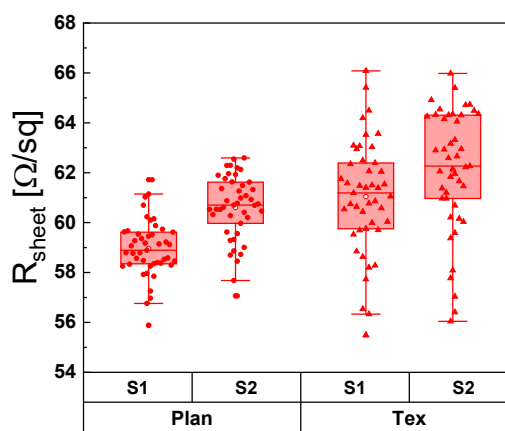
***Figure 2**: R$_{sheet}$ for 150 nm thick n$^+$ poly-Si deposited on planar and textured samples.*

3.2 Passivation properties of the *n$^+$* poly-Si layers deposited on planar and textured surface

The effective minority carrier lifetime (τ_{eff}), implied fill factor (*i*FF), saturation current density of the passivated regions ($J_{0,pass}$) and implied open-circuit voltage (*i*V_{oc}) of 150-nm *n$^+$* poly-Si test structures on planar and textured surfaces are measured using QSSPC. The measured data are shown in Figure 3. It can be seen that, on average, the passivation properties on the textured samples are inferior to those observed on planar samples. There are multiple reasons for this difference in passivation properties. The textured surface has a higher density of defects on the surface which proves more difficult to passivate than the planar surface. The SiO$_x$ layer grown on textured surfaces is known to be non-uniform, especially at the edges of the pyramids due to the dependence of the oxide growth on the orientation of the wafer. The size and distribution of the pyramids could also influence the passivation behavior. Hence, the textured surface is also expected to exhibit poorer surface passivation with a poly-Si based passivated contact.
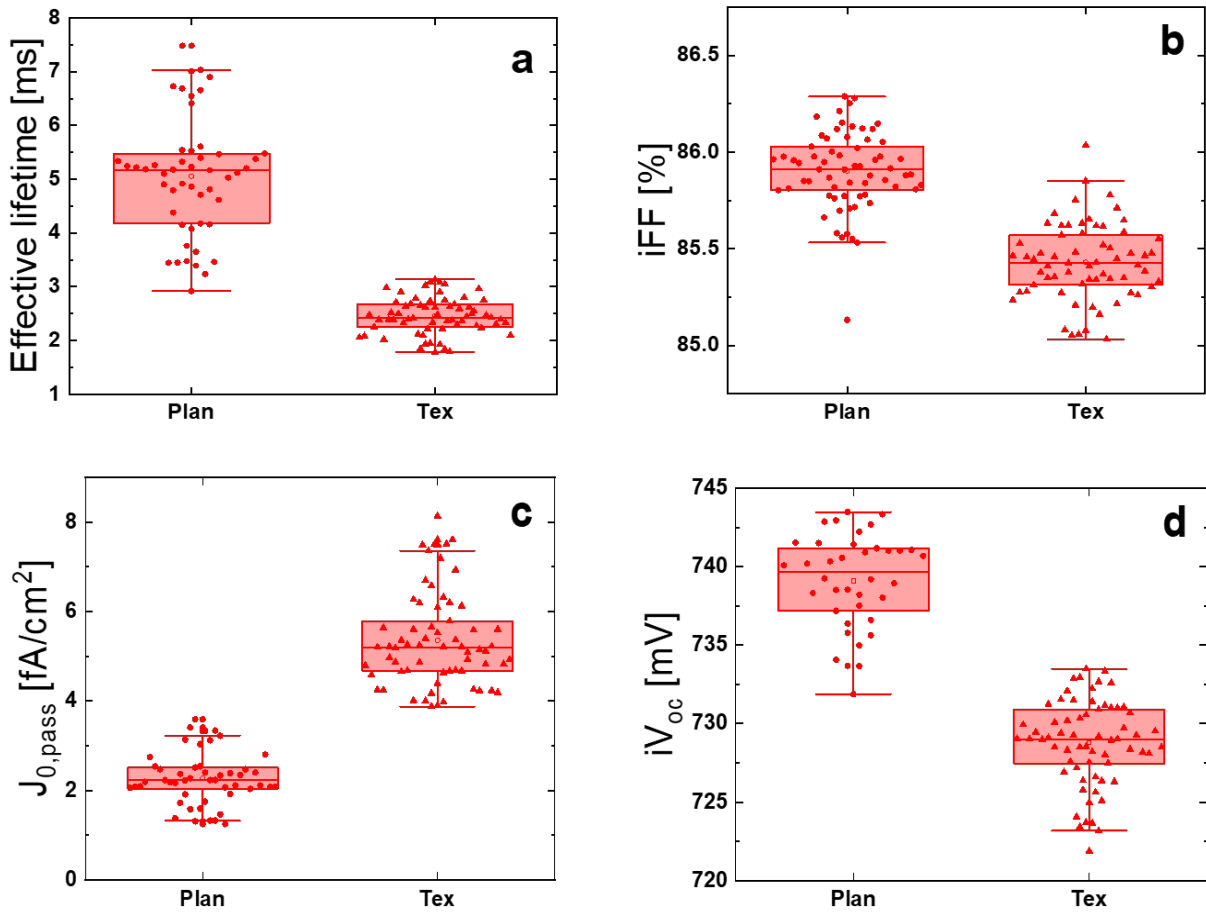
Figure 3*: QSSPC derived passivation properties of 150-nm n^+ poly-Si layers deposited on planar and textured samples. The resistivity of the n-type wafers used for preparing the samples was 1.2±0.2 Ω-cm*

3.3 Impact of surface texture on the metallization properties of FT Ag contact

The effect of the surface morphology on ρ_c is identified using TLM measurements, with contacts on planar surfaces ranging between 0.4 - 1.1 mΩ-cm^2 and 0.3 - 0.6 mΩ-cm^2 for textured surfaces, as shown in Figure 4. This corresponds to an improvement of 50%. The reduction in rear contact ρ_c leads to lower R_s and an improved FF.
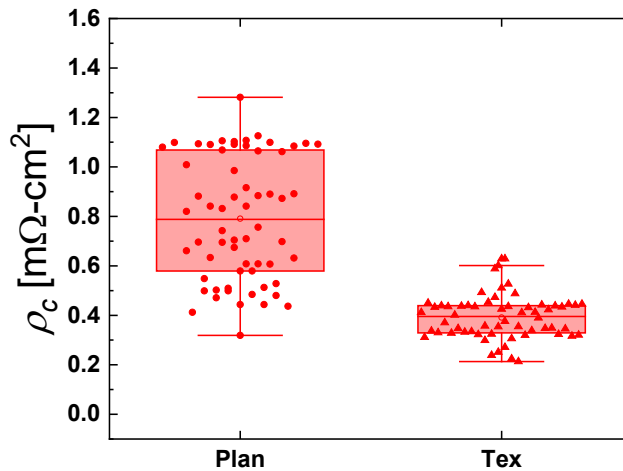
Figure 4: *ρ_c of FT Ag contacts on 150-nm n^+ poly-Si layers deposited on planar and textured samples.*

The bulk metal was etched off in a HNO_3 solution and the glass layers covering a planar and a textured surface were imaged using a SEM, see Fig. 5. Differences in the two samples were not easily discernible on visual observation. Hence, the percentage of area covered by the glass layer was estimated with ImageJ. The area percentage was calculated for 20 images.
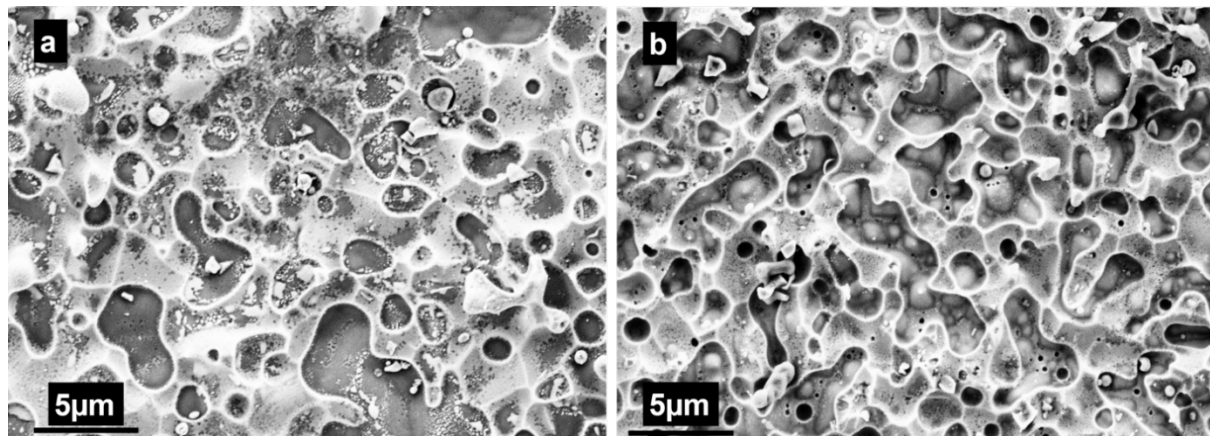

Figure 5: *SEM images of glass layers covering the surface of (a) planar and (b) textured surfaces with 150 nm thick n^+ poly-Si.*

The percentage area coverage by the glass layer on textured samples is slightly lower than that covered on the planar sample (~ 10% relative reduction, see Fig. 6). The smaller area covered by the glass layer in the case of the textured surface could lead to more crystallite formation on the textured samples, which can help explain the reduced ρ_c of textured surfaces.
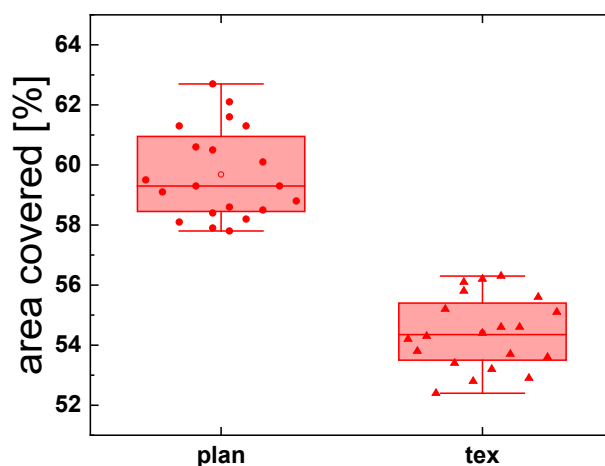

Figure 6: *Percentage area covered by the glass layer on planar and textured surfaces.*

Figure 7 shows SEM images of Ag crystallites on planar and textured surfaces. Some differences can be observed in the manner of crystallite formation. On the planar surface, the crystallites are smaller, while on the textured surface they can be seen to form small clumps. Although image analysis by ImageJ revealed almost the same percentage of area covered by the crystallites on both surfaces, the crystallites were found to be concentrated on the tips of the pyramids rather than in the valleys. However, it was speculated earlier that for textured surfaces the concentration of dopants could be highest at the tips of the textured surface [19], and since the contacts on a textured surface are usually formed at the tips of the pyramids [20], it could lead to preferential formation of crystallites on the tips of the pyramids. This could also lead to the improved values of ρ_c on the textured surface.
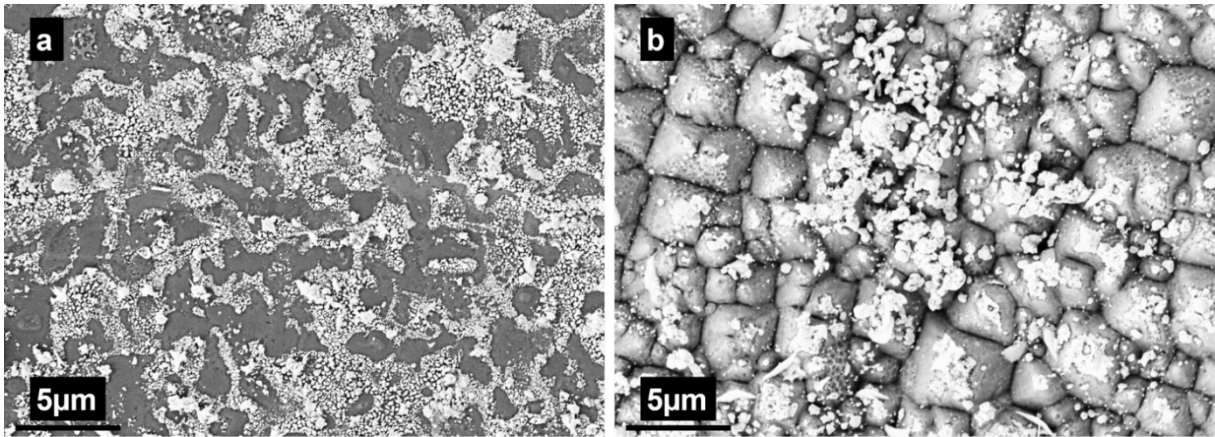
Figure 7: *Ag crystallites observed on poly-Si for (a) planar and (b) textured surfaces.*

The $J_{0,metal}$ of FT Ag contacts on planar and textured surfaces covered with n^+ poly-Si was analyzed. The values of $J_{0,metal}$ on planar and textured surfaces deduced from FEM modelling are listed in Table 1. The values of $J_{0,pass}$ obtained via simulation are also listed alongside the $J_{0,pass}$ measured by QSSPC. The simulated and measured values of $J_{0,pass}$ agree well. The $J_{0,metal}$ for textured surfaces, although slightly higher, is within the same order of magnitude as for planar surfaces.

Table 1. *$J_{0,metal}$ and $J_{0,pass}$ (measured and simulated) for FT Ag contacts on textured and planar n^+ poly-Si surfaces.*

Surface morphology	Measured [fA/cm^2]	Modelled [fA/cm^2]	
	$J_{0,pass}$	$J_{0,pass}$	$J_{0,metal}$
Planar	2.5 ± 1.3	3.2 ± 0.6	32 ± 5
Textured	5.4 ± 2.0	7.3 ± 1.2	55 ± 7

SEM images of the etch pits formed by the metal crystallites on the planar and textured surfaces are shown in Figure 8. The etch pits on a planar surface did not cause extensive damage and the poly-Si layer was found intact everywhere. However, the poly-Si damage on a textured surface was more prominent on the pyramid tips and there were certain locations where the poly-Si was completely etched off. However, no etch pits were observed on the exposed c-Si surface for textured wafers (Figure 8-b). Although the metal crystallites almost consumed the entire poly-Si layer during the contact formation process, the etching was not aggressive enough to cause extensive damage to the poly-Si and allow the crystallites to embed deep into the c-Si surface. The damage to the poly-Si was almost exclusively limited to the tips of the pyramids. This could be due to the difference in the thickness of glass layer and poly-Si at the base and at the tips of the pyramids, as it was observed by SEM that the glass layer is thinner at the tips of the pyramids than at the base. Despite the partial etching of the poly-Si layer at the pyramid tips, the $J_{0,metal}$ does not increase considerably.
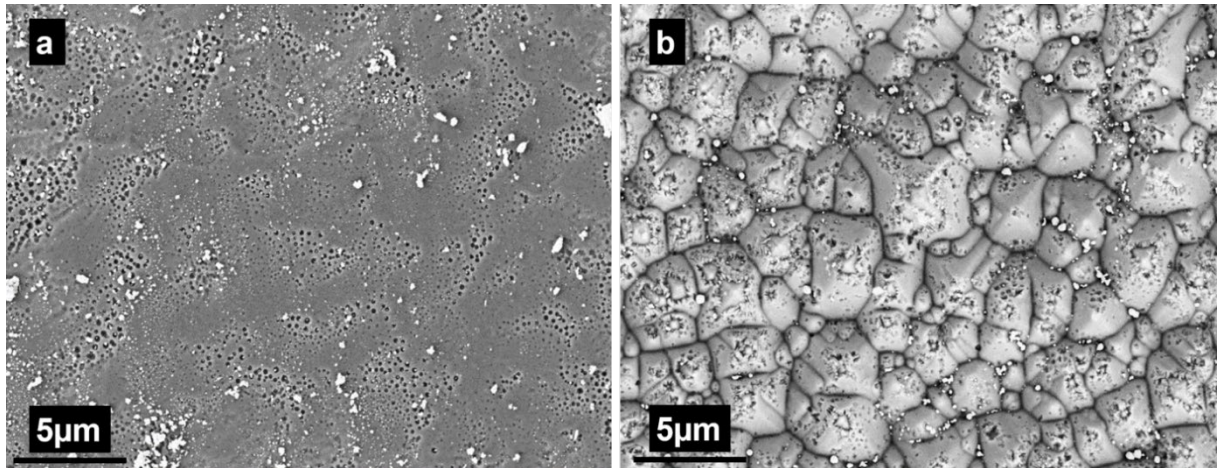
Figure 8: *SEM images of etch pits formed in poly-Si layers on (a) planar and (b) textured surfaces.*

3.4 Impact of surface texture on the performance of solar cells with rear-side passivating contact

The 1-Sun J-V parameters of large-area solar cells with n^+ poly-Si based passivating contacts on the rear side are shown in Fig. 9 a-d. It was seen that the solar cells with both side textured surface were limited by their V_{oc}. While the iV_{oc} of the symmetrical samples exhibited a difference of 15-20 mV, the V_{oc} of the solar cells with both sides textured differed by 20-25 mV. The increase in the V_{oc} loss could be attributed to the increased J_0 under the passivated regions and under the metal contacts for textured surface. The fill factor showed improvements in line with the observations regarding the contact resistivity. J_{sc} was also observed to be slightly lower (≈ 0.2 mA/cm^2) in the double-side textured samples as compared to the single-side textured samples. The improvement in the fill factor could not compensate for the losses in the V_{oc} and J_{sc}, and as a result the efficiency of the solar cells with double-side textured surfaces was lower than that of those with only one side textured.
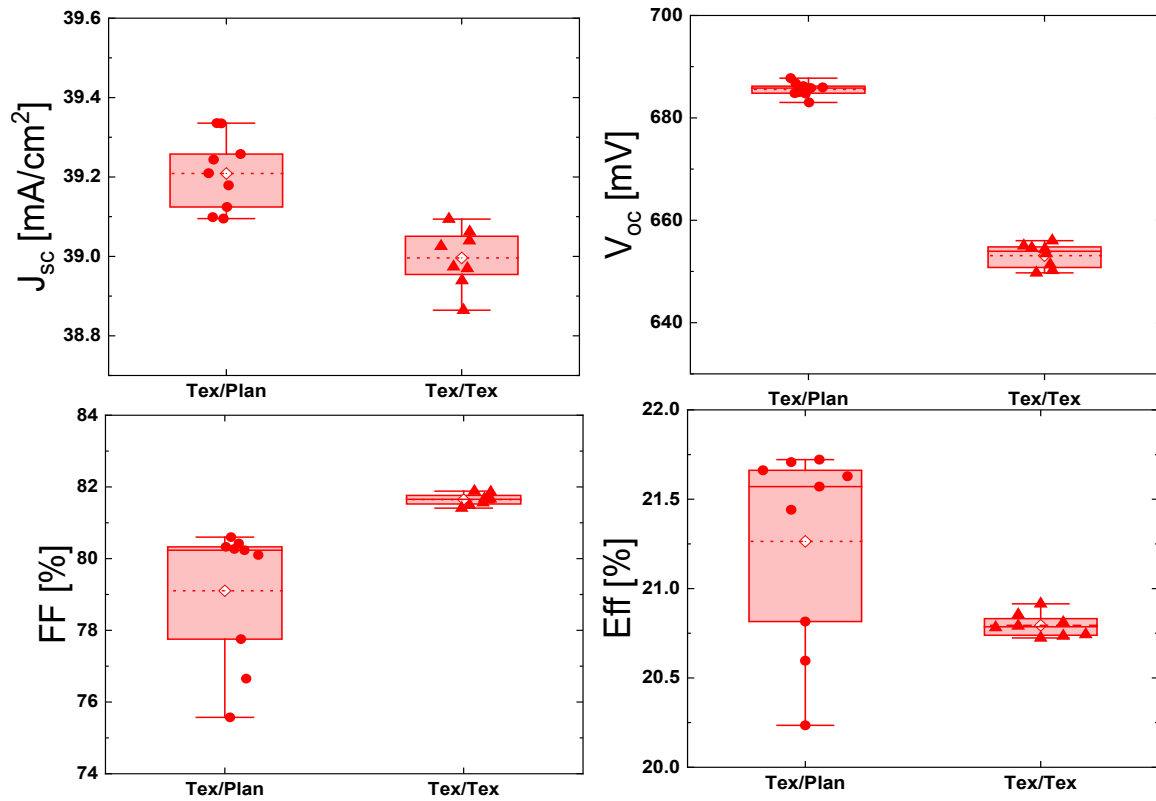
Figure 9: *One-Sun J-V parameters of solar cells formed with single-side poly-Si based passivating contacts on the planar and textured rear side.*

4. Modelling and Simulations of the solar cells

The impact of the surface morphology on the short-circuit current density was further investigated with the help of a SunSolve model. The solar cells with different rear surfaces were modelled and a loss analysis was done. The cross-sectional schematics of the solar cells are shown in Figure 10. The simulation shows that the loss in the J_{sc} likely arose from the parasitic absorption in the rear poly-Si layer. This can be attributed to the non-uniform thickness of the poly-Si layer deposited on the textured surface, as compared to the planar surface. The J_{sc} loss comparison for the two types of solar cells is shown schematically in Figure 11. Though the losses due to the front escape are reduced, the parasitic absorption, together with the slightly lower generated current in the bulk, resulted in overall lower J_{sc} values. We would like to point here that the measurements were carried on a J-V tester with a copper chuck and single-side illumination. The bifaciality of the solar cells with both sides textured surface was simulated to be slightly higher ($\approx$ 0.68) than that with planar surface on the rear side ($\approx$ 0.65).
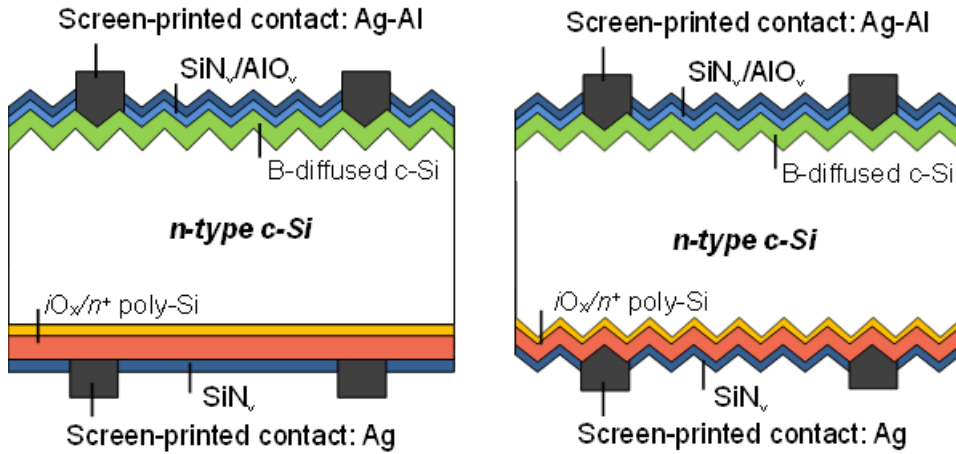
Figure 10: *Solar cell schematics with (left) planar rear surface and (right) textured rear surface.*
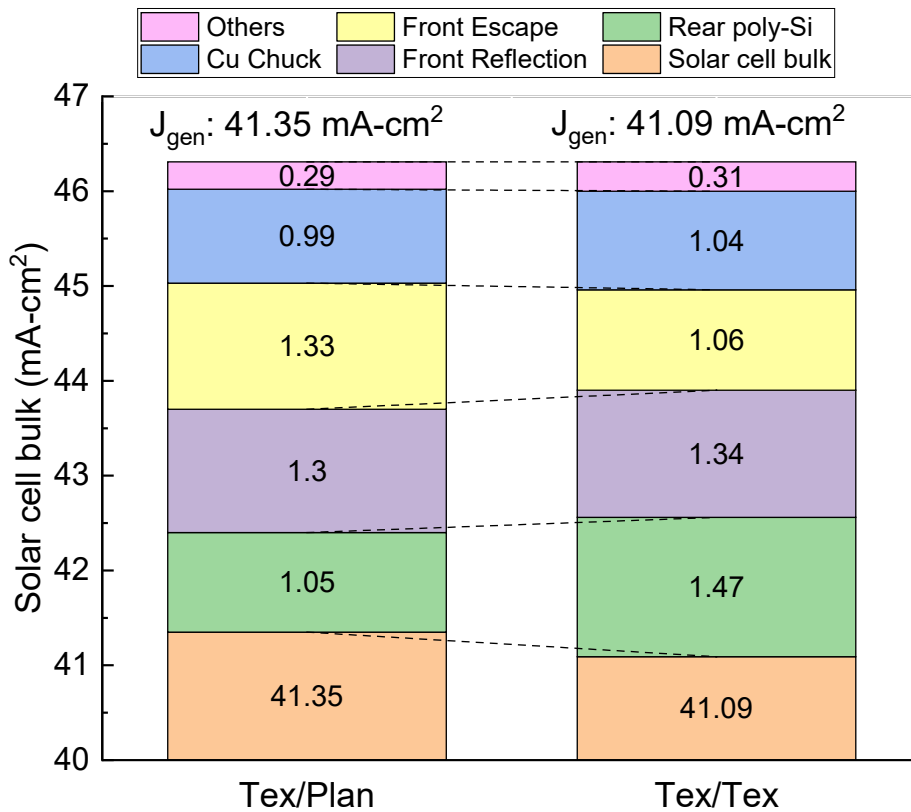

Figure 11: *J_{sc} loss components shown schematically using the results obtained from SunSolve modelling of solar cells with planar rear (left) and textured rear surface (right).*

Further simulations of the solar cells were carried out with the Quokka V2 software [21]. The data used as input for the model are shown in Table 2.

Table 2. *Input parameters for the solar cell simulations using Quokka-2.*

	Parameter	n^+ poly-Si Tex/Plan	n^+ poly-Si Tex/Tex	
Simulated LIV	V_{oc} [mV]	696	696	
	J_{sc} [mA/cm^2]	41.2	40.8	
	FF [%]	78.3	78.4	
	Efficiency [%]	22.4	22.3	
Front boron emitter	Gridline number	101	101	Front screen printing parameters
	Gridline width [µm]	35	35	
	Gridline height [µm]	20	20	
	Floating busbar? (Y/N)	Y	Y	
	Busbar number	5	5	
	Busbar width [µm]	0	0	
	Busbar height [µm]	0	0	
	Metal fraction [%]	2.55	2.55	
	$R_{sheet,poly}$ [Ω/□]	150	150	Front surface field parameters
	ρ_c [mΩ-cm^2]	10	10	
	$J_{0e,pass}$ [fA/cm^2]	18	18	
	$J_{0e,metal}$ [fA/cm^2]	1400	1400	
	$J_{0e,total}$ [fA/cm^2]	53.726	53.726	
Bulk	Doping type	n-type	n-type	Bulk parameters
	Thickness [µm]	150	150	
	ρ_{bulk} [Ω-cm]	2	2	
	τ_{n0} (= τ_{p0}) [ms]	1	1	
Rear n^+ poly-Si	Gridline number	190	190	Back surface field parameters
	Gridline width [µm]	35	35	
	Gridline height [µm]	25	25	
	Floating busbar? (Y/N)	N	N	
	Busbar number	0	0	
	Busbar width [µm]	-	-	
	Metal fraction [%]	6.38	6.38	
	Poly-Si thickness [nm]	100	100	
	$R_{sheet,poly}$ [Ω/□]	100	100	
	ρ_c [mΩ-cm^2]	2	1	
	$J_{0b',pass}$ [fA/cm^2]	1	1	
	$J_{0b',metal}$ [fA/cm^2]	28	35	
	$J_{0b',total}$ [fA/cm^2]	2.914	2.914	
Etc.	Ag/Al paste resistivity [µΩ-cm]	-	-	External circuit / Generation current
	External $R_{s'}$ [Ω-cm^2]	0.147	0.147	
	Generation Profile (Zeta) from Sunsolve	tx_pl.csv	tx_tx.csv	
	J_{gen} [mA/cm^2] - Disabled	41.35	41.09	

The model was used to calculate the Free Energy Loss analysis (FELA) at the 1-Sun maximum power point (MPP). The simulated J-V curves for the two types of solar cell are shown in Figure 12. It is seen that the theoretical models do not exhibit any loss in the V_{oc} due to the texturing of the rear surface. This was also visible in the symmetrical samples. However, due to reasons not yet fully understood, the textured rear surface resulted in significant V_{oc} loss in the fabricated solar cells.
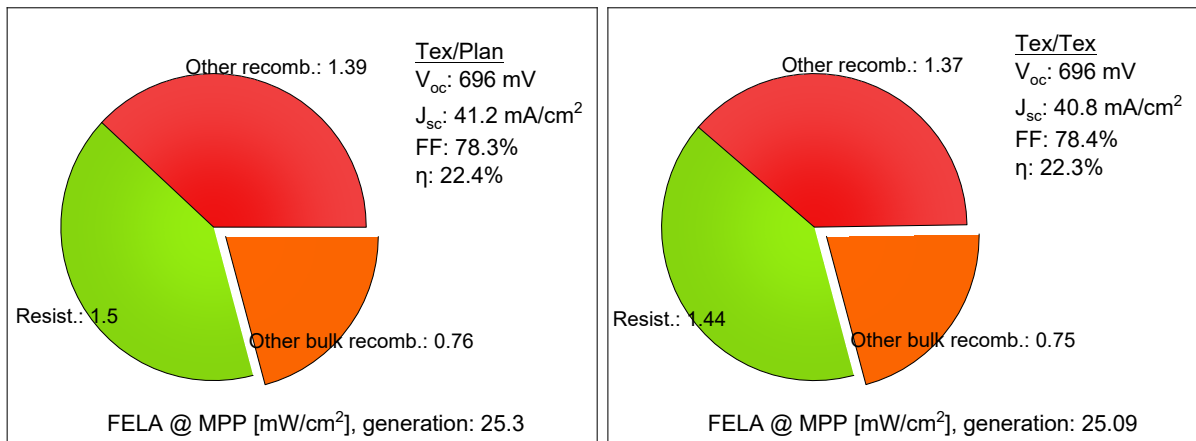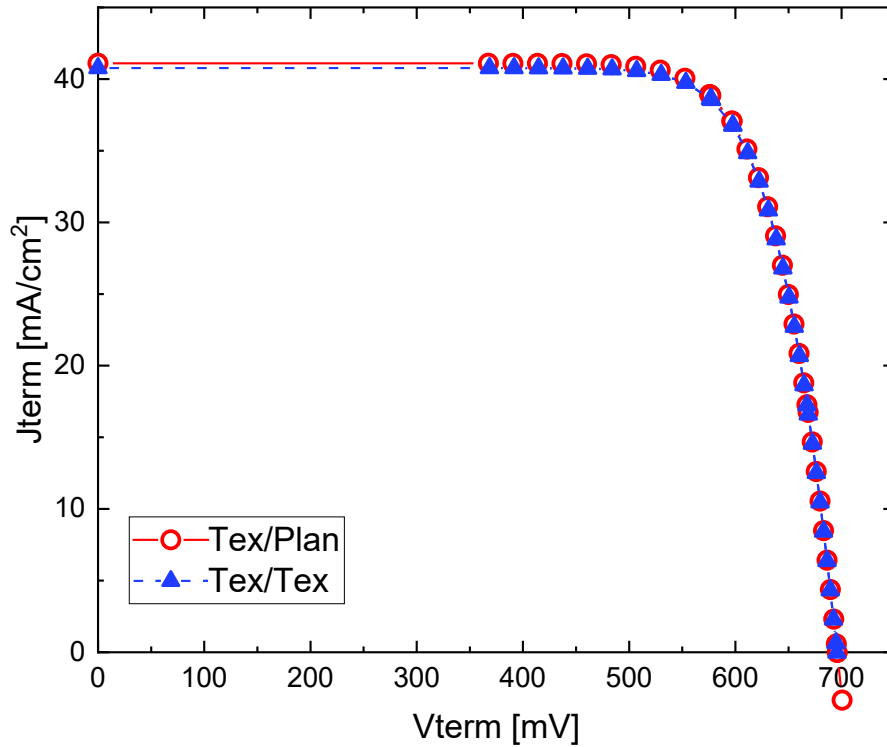

Figure 12: *(Top) Quokka-2 simulated 1-Sun J-V curves of solar cells with planar rear surface and textured rear surface. (Bottom) FELA plots of the cell with planar rear surface (left) and textured rear surface (right).*

5. Conclusion

In this work we studied in detail the impact of texturing the rear surface on the performance of single-side poly-Si based passivated contact solar cells. The impact of the surface texturing on the behaviour of the metal contacts was researched in depth. With the help of symmetrical samples, it was shown that the textured surface did not significantly impact the passivation of

the surface by the iO_x/n^+ poly-Si layer. The contact resistivity was found to be lower for the textured surface. On further investigation of the SEM images of the metallized glass layer and analyzing the images using ImageJ it was found that the improvement in the contact properties was due to the less glass covering the surface after metallization. The number of metal crystallites was also found to be concentrated on the tips of the pyramids. Both these observations could be the reason for the improved contact resistivity observed on textured surfaces. However, the $J_{0,metal}$ was not found to be adversely impacted by the textured surface, and the values for both planar and textured surfaces were quite similar. Despite this, the solar cells fabricated with planar and textured rear surfaces exhibited a considerable difference in the 1-Sun performance. Although the FF improved for the solar cells with textured rear surface, the V_{oc} deteriorated considerably, resulting in an efficiency loss of $\approx 0.8\%$ absolute. Simulations using SunSolve showed that the J_{sc} of the double-side textured solar cell is slightly lower than for the single-side textured cell. However, the loss in J_{sc} can potentially be recovered in field applications as these are bifacial solar cells by design. Additional device modelling using Quokka-2 showed a small loss in free energy at the 1-Sun MPP due to the textured rear surface. Further research on minimizing the V_{oc} loss of the fabricated solar cells might help improve the efficiency of the double-side textured devices.

Data availability statement

Most of the data used for the current work has been included in the manuscript. Any additional data can be made available upon request to the authors.

Author contributions

P. Padhamnath was responsible for the conceptualization, investigation, formal analysis and validation of the experiments and the writing of the original draft. J.D. Arcebal was responsible for the investigation, visualization, validation and formal analysis of the experiments and helped with the writing of the original draft. S. Dasgupta and G. De Luna helped with the investigation, visualization and validation of the data and results. A. Rohatgi and A.G. Aberle were responsible for funding acquisition, project administration, provision of resources and for reviewing and editing the manuscript.

Competing interests

The authors declare that they have no competing interests.

Acknowledgement

Legal Disclaimer

The views expressed herein do not necessarily represent the views of the U.S. Department of Energy, the United States Government, National Research Foundation Singapore (NRF), the Energy Market Authority of Singapore (EMA) and Singapore Economic Development Board (EDB).

References

1. Nandakumar, N., et al., Approaching 23% with large-area monoPoly cells using screen-printed and fired rear passivating contacts fabricated by inline PECVD. PIP, 2019. **27**(2): p. 107-112,doi: https://doi-org.libproxy1.nus.edu.sg/10.1002/pip.3097.

2. Mertens, V., et al., Plasma enhanced chemical vapor-deposited $SiO_x(N_y)$/n-type polysilicon on oxide passivating contacts in industrial back-contacted Si solar cells. Solar RRL, doi: https://doi-org.libproxy1.nus.edu.sg/10.1002/solr.202300919.

3. Padhamnath, P., et al., Progress with passivation and screen-printed metallization of Boron-doped monoPoly™ layers. Solar Energy, 2022. **231**: p. 8-26, doi: https://doi.org/10.1016/j.solener.2021.11.015.

4. Padhamnath, P., et al., High-quality doped polycrystalline silicon using low-pressure chemical vapor deposition (LPCVD). Energy Procedia, 2018. **150**: p. 9-14, doi: https://doi.org/10.1016/j.egypro.2018.09.014.

5. Reiter, S., et al., Parasitic absorption in polycrystalline Si-layers for carrier-selective front junctions. Energy Procedia, 2016. **92**: p. 199-204, doi: https://doi.org/10.1016/j.egypro.2016.07.057.

6. Padhamnath, P., et al., Optoelectrical properties of high-performance low-pressure chemical vapor deposited phosphorus-doped polysilicon layers for passivating contact solar cells. TSF, 2020. **699**: p. 137886, doi: 10.1016/j.tsf.2020.137886.

7. Padhamnath, P., et al., Development of thin polysilicon layers for application in monoPoly™ cells with screen-printed and fired metallization. SOLMAT, 2020. **207**: p. 110358, doi: https://doi.org/10.1016/j.solmat.2019.110358.

8. Nandakumar, N., et al., Large-area monoPoly solar cells on 110 µm thin c–Si wafers with a rear n^+ poly-Si/SiO_x stack deposited by inline plasma-enhanced chemical vapour deposition. PIP,2023. **31**(4): p. 360-368, doi: https://doi-org.libproxy1.nus.edu.sg/10.1002/pip.3555.

9. Padhamnath, P., et al., Design, development and analysis of large-area industrial silicon solar cells featuring a full area polysilicon based passivating contact on the rear and selective passivating contacts on the front. SOLMAT, 2023. **256**: p. 112351, doi: 10.1016/j.solmat.2023.112351.

10. Zhong, R., et al., Detailed investigation of electrical and optical properties of textured n-type and roughened p-type tunnel oxide passivated contacts for screen-printed double-side passivated contact silicon solar cell application. TSF, 2023. **783**: p. 140046, doi: https://doi.org/10.1016/j.tsf.2023.140046.

11. Padhamnath, P., et al., Design and development of front and back contact solar cells with selective poly-Si passivating contact on the front and local Al contact on the rear. SOLMAT, 2024. **269**: p. 112759, doi: 10.1016/j.solmat.2024.112759.

12. Padhamnath, P., et al., Characterization of screen printed and fire-through contacts on LPCVD based passivating contacts in monoPoly™ solar cells. Solar Energy, 2020. **202**: p. 73-79, doi: https://doi.org/10.1016/j.solener.2020.03.087.

13. Padhamnath, P., et al., Metal contact recombination in monoPoly™ solar cells with screen-printed & fire-through contacts. SOLMAT, 2019. **192**: p. 109-116, doi: https://doi.org/10.1016/j.solmat.2018.12.026.

14. Padhamnath, P., et al., Impact of firing temperature on fire-through metal contacts to P-doped (n+) and B-doped (p+) poly-Si. SOLMAT, 2021. **230**: p. 111217, doi: https://doi.org/10.1016/j.solmat.2021.111217.

15. Padhamnath, P., et al. Modeling of contact resistivity of fire-through Ag-Al contacts to boron doped LPCVD polysilicon layers. AIP Conference Proceedings. 2022. **2709**: p. 020010, doi: 10.1063/5.0126042.

16. Glatthaar, R., et al., Contact Formation of Silver Paste and Atmospheric Pressure Chemical Vapor Deposition (n) Poly-Silicon Passivating Contacts on Planar and Textured Surfaces. PSS (a), 2022. **219**(24): p. 2200501, doi: https://doi-org.libproxy1.nus.edu.sg/10.1002/pssa.202200501.

17. Chaudhary, A., et al., Influence of silicon substrate surface finish on the screen-printed silver metallization of polysilicon-based passivating contacts. PSS (a), 2022. **219**(9): p. 2100869, doi: https://doi-org.libproxy1.nus.edu.sg/10.1002/pssa.202100869.

18. Guo, C., et al., Influence of backside surface morphology on passivation and contact characteristics of TOPCON solar cells. Solar Energy, 2023. **258**: p. 278-288, doi: https://doi.org/10.1016/j.solener.2023.04.065.

19. Choi, C.-J., et al. Two-dimensional dopant profiling in $POCl_3$-diffused n^+ emitter of textured silicon solar cells. in 2011 37th IEEE PVSC. 2011. IEEE, doi: 10.1109/PVSC.2011.6186542.

20. Cabrera, E., et al., Current transport in thick film Ag metallization: Direct contacts at silicon pyramid tips? Energy Procedia, 2011. **8**: p. 540-545, doi: https://doi.org/10.1016/j.egypro.2011.06.179.

21. Fell, A. and P.P. Altermatt, A detailed full-cell model of a 2018 commercial PERC solar cell in Quokka3. IEEE JPV, 2018. **8**(6): p. 1443-1448, doi: 10.1109/JPHOTOV.2018.2863548.